Supplementary Information

Triple captured iron by defect abundant NiO for efficient water oxidation

Ya-Nan Zhou, Feng-Ge Wang, Jian-Cheng Zhou, Bin Dong *, Yi-Wen Dong,

Xin Liu, Bin Liu, Jian-Feng Yu, Yong-Ming Chai *

State Key Laboratory of Heavy Oil Processing, College of Chemical Engineering, China University of Petroleum (East China), Qingdao 266580, PR China

* Corresponding author. Email: dongbin@upc.edu.cn (B. Dong); ymchai@upc.edu.cn (Y.M. Chai)

Tel: +86-532-86981156, Fax: +86-532-86981156

Table of content

Characterization

The scanning electron microscopy (SEM) (JEM 2100F) and transmission electron microscopy (TEM) (FEI Tecni G20, 200 kV) are used to characterize the morphology and structure of synthesized samples. The X-ray diffraction (XRD) with Cu Kα radiation (λ = 1.54 Å) on the Brook D8 advance equipment is applied to collect the crystal structure and phase information of the samples. X-ray photoelectron spectroscopy (XPS) is applied to analyze the surface chemical structure and valence information by Thermo Fisher K-alpha 250Xi. Raman spectrum was collected on LabRAM HR Evolution with an excitation wavelength of 514 nm. The inductively coupled plasma (ICP) spectrometer is used to detect the element contents. The specific surface area is determined on a tristar II Plus system. The defects are characterized by electron paramagnetic resonance (EPR) spectrum on electron paramagnetic resonance spectrometer (JEOL JES FA200).

Electrochemical measurements

Electrochemical performance tests were performed at room temperature through a standard three-electrode system with Gamry Reference 3000 electrochemical equipment. The cut MoNi foam (1 cm × 2 cm) was ultrasonically washed by hydrochloric acid, acetone, ethanol and deionized water, respectively, for 20 minutes to remove the surface impurity. All electrochemical measurements were conducted under the same conditions in 1 M KOH. The obtained samples, Pt plate electrode and saturated calomel electrode were selected as working electrode, counter electrode and reference electrode, respectively. The scan rate of the linear sweep voltammetry (LSV) curve was maintained at 5 mV s^{-1}. All the electrode potential were converted to reversible hydrogen electrode (RHE) via the Nernst equation: $E_{RHE} = E_{SCE} +$

0.0592 pH + E^0_{SCE} (E^0_{SCE} = 0.245 V). The CV curves with different scanning rates are employed to determine the double-layer capacitances (C_{dl}). The stability of the sample was evaluated via both chronoamperometry and fast CV cycles with a rate of 40 mV s^{-1} for 3000 sweeps. The frequency of electrochemical impedance spectroscopy (EIS) was range from 10^5 Hz to 0.1 Hz at 0.20 V vs. SCE with an AC voltage of 5 mV. The activation of samples is performed by the LSV scan with a scan rate of 10 mV s^{-1}.

Density functional theory calculations

The density functional theory (DFT) calculations were performed using the Materials Studio software. The exchange-correlation interaction was described by generalized gradient approximation (GGA) with the Perdew-Burke-Ernzerhof (PBE) functional.[1-3] The energy cutoff was set to 570 eV. The Monkhorst-Pack k-point mesh was set as 3 × 3 × 6, 3 × 3 × 5, 3 × 3 × 5 and 3 × 3 × 5 for NiO, Fe-NiO, NiOOH and Fe-NiOOH models, respectively. The convergence criterion in geometry optimization was set as 10^{-5} eV/atom for energy.

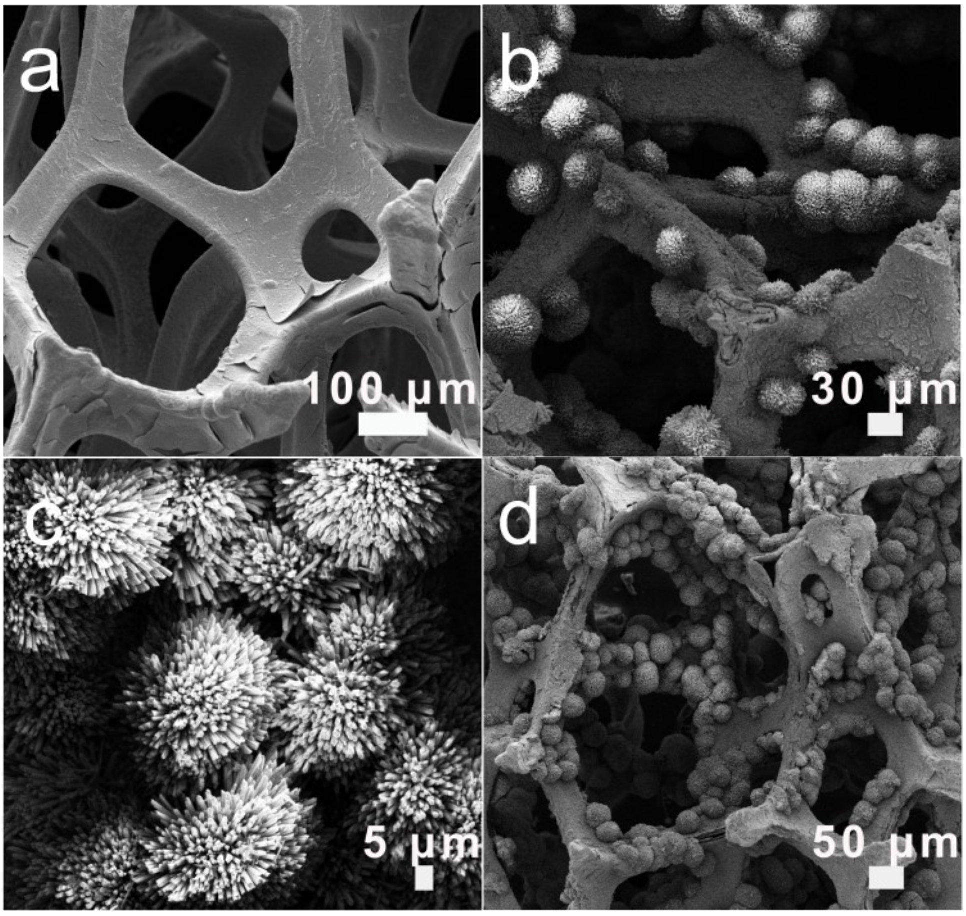

Fig. S1 SEM morphologies of (a) MoNi foam, (b and c) $NiMoO_4$@NiO. (d) Fe-$NiMoO_4$@NiO-30.

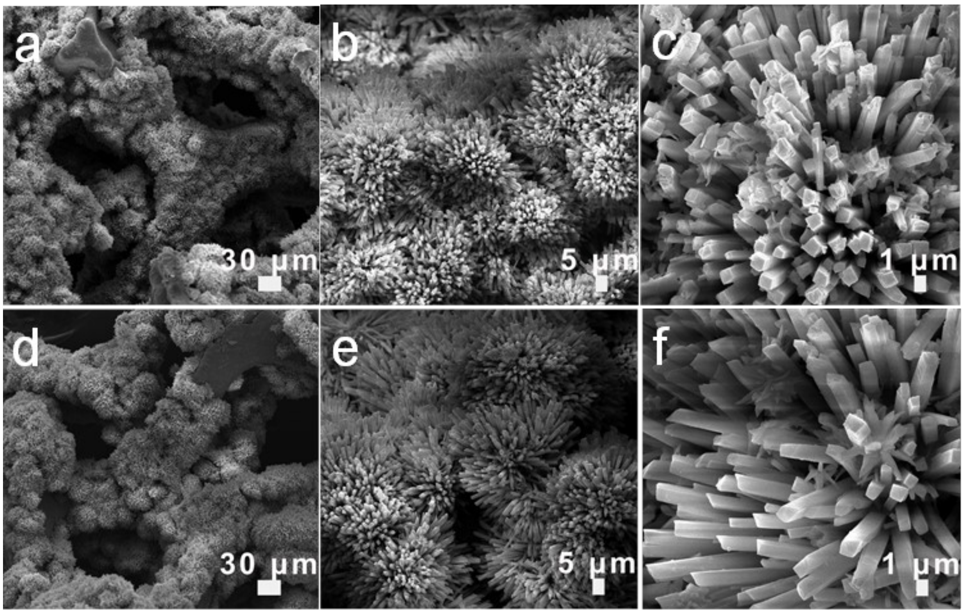

Fig. S2 SEM morphologies of (a-c) Fe-$NiMoO_4$@NiO-50 and (d-f) Fe-$NiMoO_4$@NiO-5.

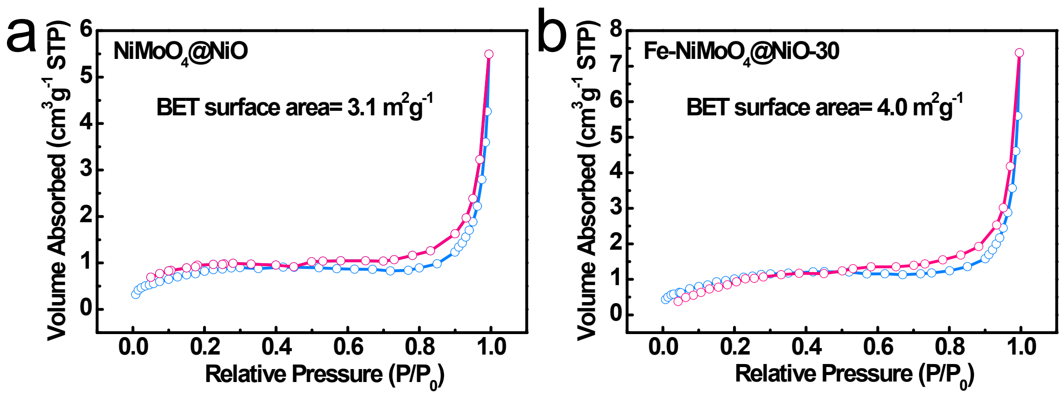

Fig. S3 N_2 adsorption-desorption isotherm of $NiMoO_4$@NiO and Fe-$NiMoO_4$@NiO-30.

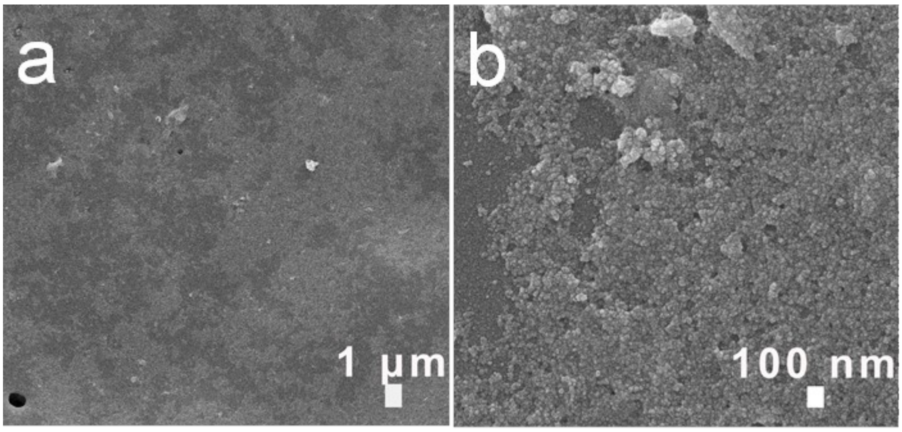

Fig. S4 SEM morphologies of Fe-Fe_2MoO_4-30 sample.

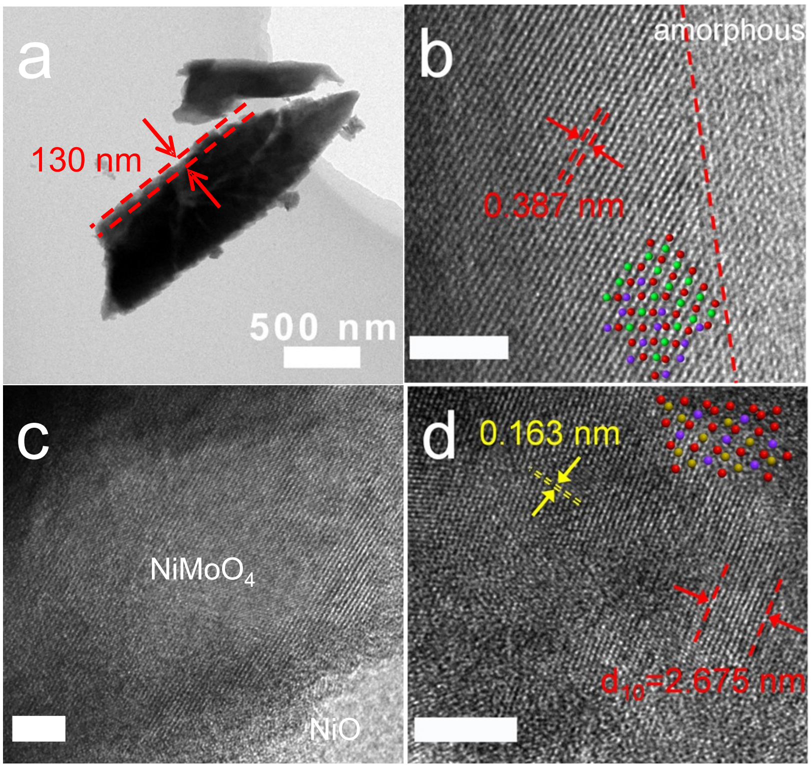

Fig. S5 (a) TEM image and (b) HRTEM image of $NiMoO_4$@NiO precursor, HRTEM image of (c) Fe-$NiMoO_4$@NiO-30 and (d) Fe-Fe_2MoO_4-30 sample. Two distinguishable lattices with interplanar spacing of 0.163 nm and 0.267 nm, corresponding to the (511) plane of Fe_2MoO_4 and (101) plane of MoO_3, respectively. Scale bar: 5 nm. Insert: the illustration of crystal lattice of $NiMoO_4$/NiO interface (b) and Fe_2MoO_4. Red ball: O; green ball: Ni; purple ball: Mo; brown ball: Fe.

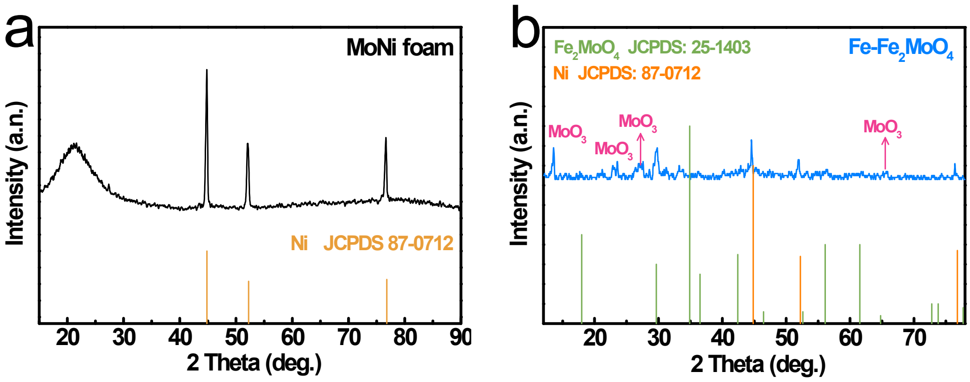

Fig. S6 XRD pattern of (a) Commercial MoNi foam and (b) Fe-Fe_2MoO_4.

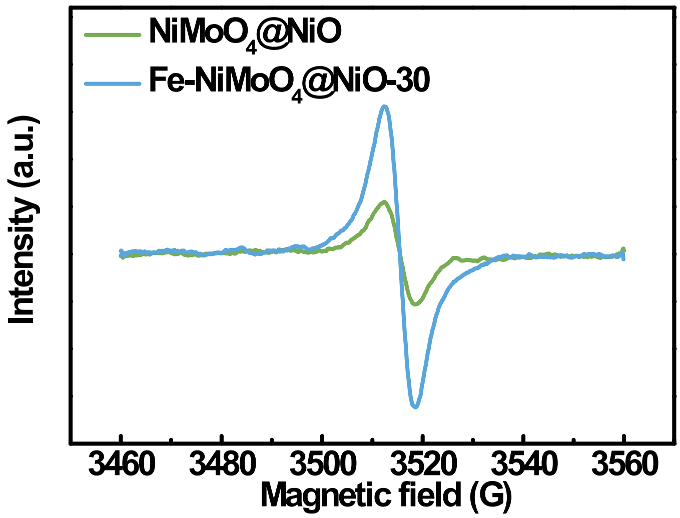

Fig. S7 EPR spectra of $NiMoO_4$@NiO and Fe-$NiMoO_4$@NiO-30.

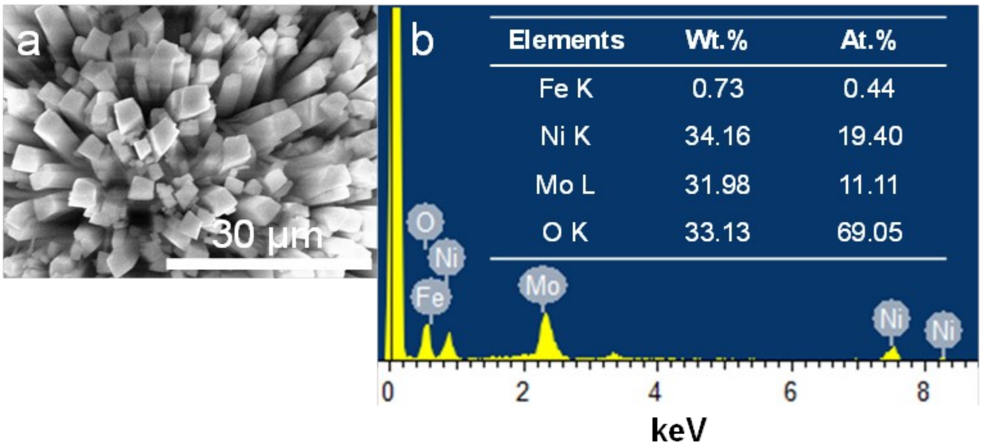

Fig. S8 (a) SEM image and (b) Corresponding element contents of Fe-$NiMoO_4$@NiO-30.

Table S1 Element contents of Fe, Ni, Mo and O detected by EDS in Fe-$NiMoO_4$@NiO-5 and Fe-$NiMoO_4$@NiO-50 samples.

	Fe-$NiMoO_4$@NiO-5		Fe-$NiMoO_4$@NiO-50	
Element	At.%	Wt.%	At.%	Wt.%
Fe K	0.34	0.58	0.70	1.18
Ni K	18.19	32.33	23.44	41.38
Mo L	11.41	33.15	8.72	25.14
O K	70.06	33.94	67.14	32.30
Total account	100.00	100.00	100.00	100.00

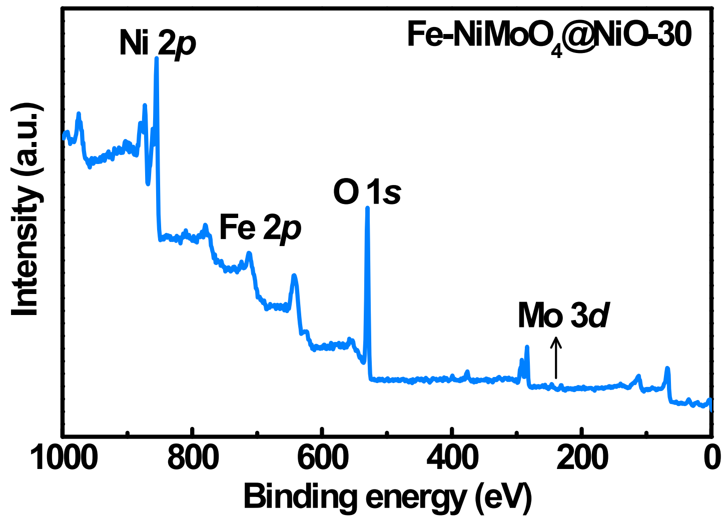

Fig. S9 XPS survey scan of Fe-NiMoO$_4$@NiO-30 sample, where the Mo, Ni, Fe, O elements can be clearly indexed.

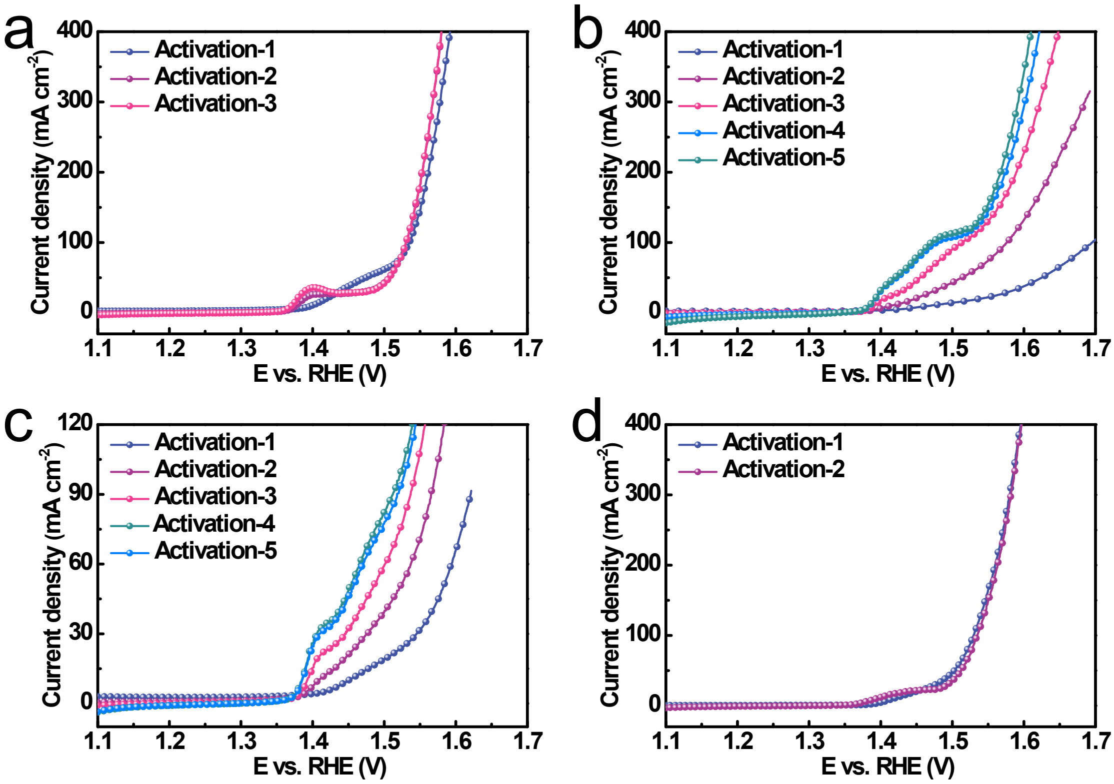

Fig. S10 Electrochemical activation of (a) NiMoO$_4$@NiO, (b) Fe-NiMoO$_4$@NiO-5, (c) Fe-NiMoO$_4$@NiO-50 and (d) Fe-Fe$_2$MoO$_4$ by LSV scan, where “1, 2 …” means “first scan, second scan…”

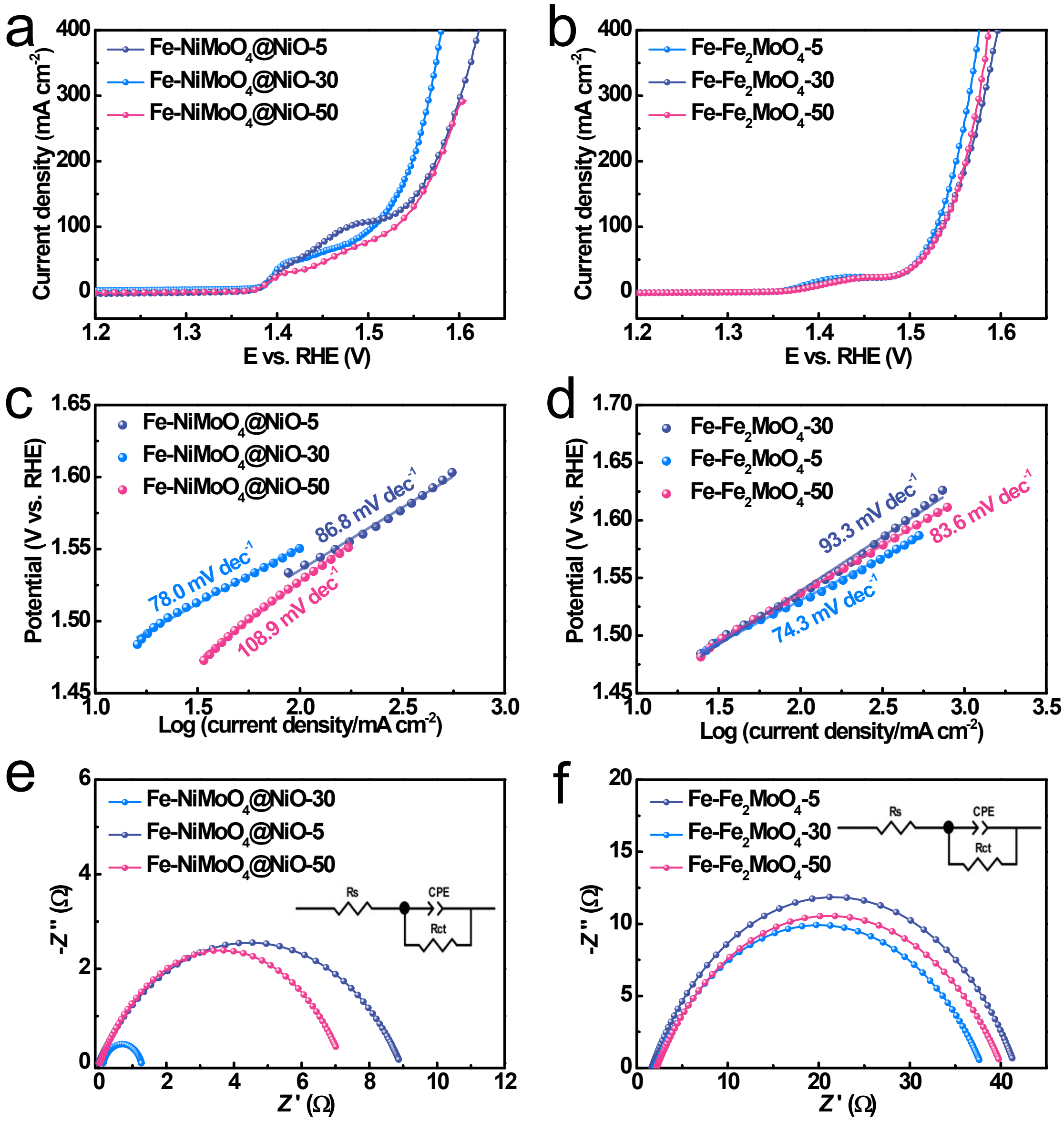

Fig. S11 Electrochemical activity of Fe-$NiMoO_4$@NiO-*t* and Fe-Fe_2MoO_4-*t*. (a and b) LSV curves, (c and d) Tafel plots, (e and f) EIS plots.

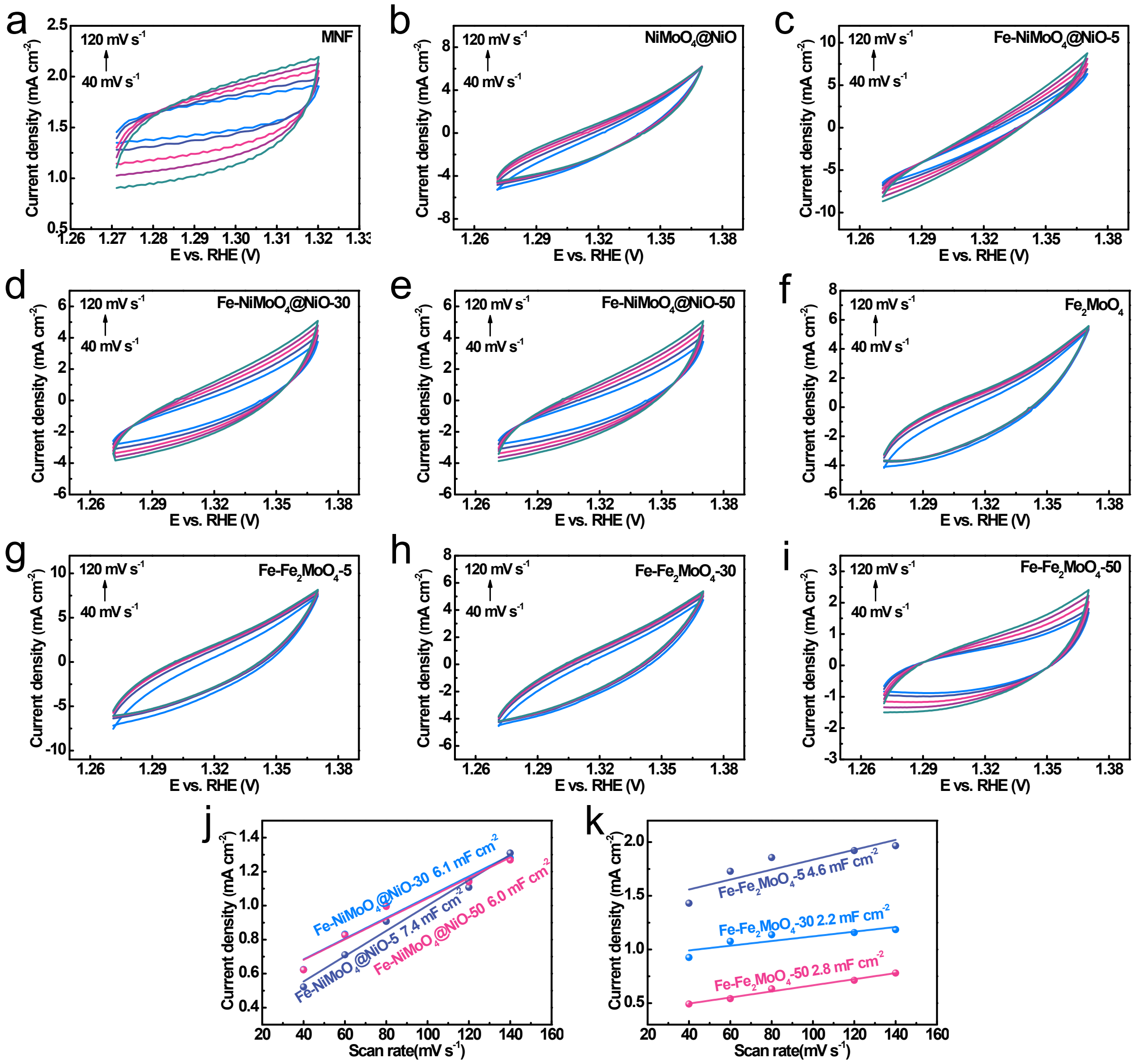

Fig. S12 (a-i) CV cycles of all the obtained samples with scan rate of 40, 60, 80, 100, 120 mV s^{-1} and corresponding C_{dl} value (j and k).

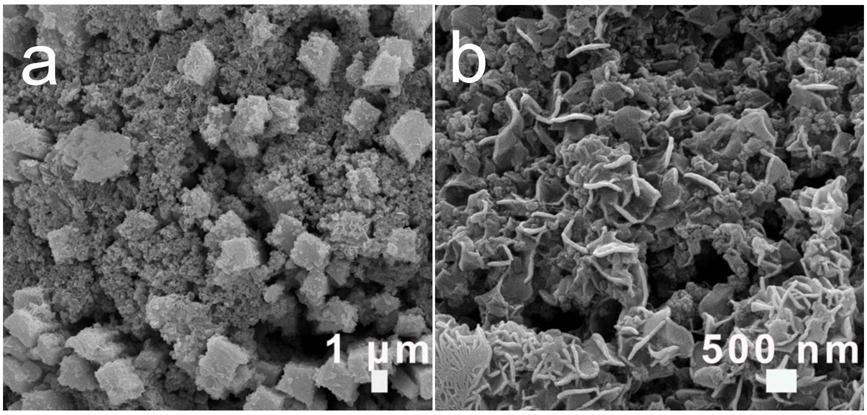

Fig. S13 SEM morphologies of Fe-$NiMoO_4$@NiO-30 after long-term stability of 35 h.

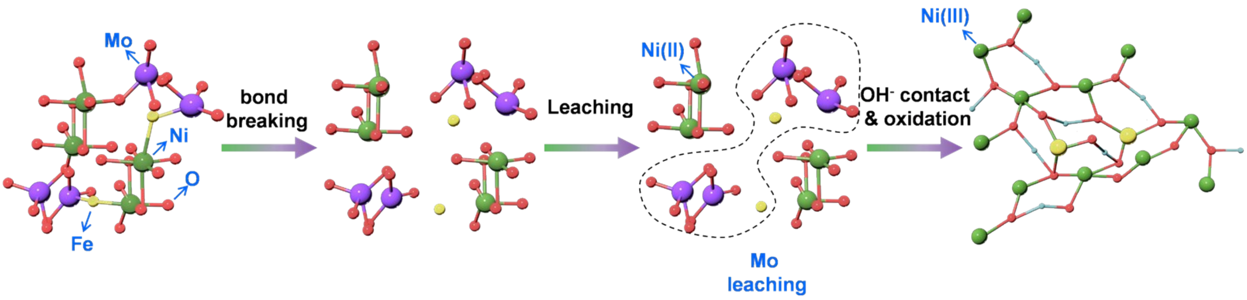

Fig. S14 Reconstruction process diagram of Fe-$NiMoO_4$@NiO-30.

Table S2 ICP content result of KOH (1 M) electrolyte for Fe-$NiMoO_4$@NiO-30 and Fe-Fe_2MoO_4-30 before and after long-term stability.

	Fe (mg/L)		Ni (mg/L)		Mo (mg/L)	
Fe-$NiMoO_4$@NiO-30	Before	After	Before	After	Before	After
	0.46	0.04	0.026	0.07	0.10	1459.61
Fe-Fe_2MoO_4-30	Before	After	Before	After		
	0.46	1.20	0.026	33.77		

Table S3 Comparison of the OER activity of Fe-$NiMoO_4$@NiO-30 with the other OER electrocatalysts in 1 M KOH.

Electrocatalyst	j (mA cm^{-2})	η (mV)	b (mV dec^{-1})	Ref.
Fe-$NiMoO_4$@NiO-30	100	274	78.0	**This work**
Fe-$NiMoO_4$	100	350	90.0	**[4]**
Co_3S_4@$NiMoO_4$	100	620	102.0	**[5]**
$NiCo_2O_4$@$NiMoO_4$/NF	100	522	117.6	**[6]**
$NiCo_2O_4$@$NiMoO_4$	100	413	94.1	**[7]**
$NiMoO_4$	100	338	48.0	**[8]**
NM-FC2	100	383	71.8	**[9]**
CeO_2-$NiMoO_4$	100	346	79.0	**[10]**
***a*-NiFeMo**	30	321	49.0	**[11]**
SELF-RECONCAT	100	290	66.6	**[12]**
CR-NiOOH	100	308	-	**[13]**
NiFeMo-N_2	100	285	26.7	**[14]**
$NiCoFeO_x$ NHS	100	404	58.0	**[15]**
NiFeMo	100	593	35.0	**[16]**
NiFeMo	100	278	59.9	**[17]**
NiFeMo/NF	100	280	42.7	**[18]**
NiFeMoS/NF-P	100	285	69.0	**[19]**

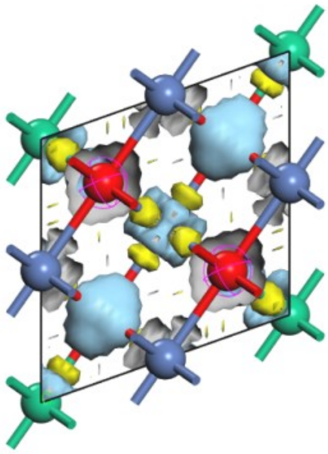

Fig. S15 The electron density difference of Fe-$NiMoO_4$@NiO-30. The blue and yellow represent the increase and decrease of electron density, respectively.

Reference

1 Y. Dong, P.X. Zhang, Z.Y. Yang, Y.P. Li and X.M. Sun, A First-Principles Study of Oxygen Formation Over NiFe-Layered Double Hydroxides Surface, *Catal. Lett.*, 2015, **145**, 1541–1548.

2 M. Bajdich, M. García-Mota, A. Vojvodic, J.K. Nørskov and A.T. Bell, Theoretical Investigation of the Activity of Cobalt Oxides for the Electrochemical Oxidation of Water, *J. Am. Chem. Soc.*, 2013, **135**, 13521–13530.

3 J. Perdew, J.A. Chevary, S.H. Vosko, K. Jackson, M. Pederson, D.J. Singh and C. Fiolhais, Atoms, molecules, solids, and surfaces: Applications of the generalized gradient approximation for exchange and correlation, *Phys. Rev. B*, 1992, **46**, 6671.

4 Z.X. Yin, S. Zhang, W. Chen, M.X. zhi, Y. Zhou, Z.F. Zhang, X. Wang and J.L. Li, Hybrid-atom-doped $NiMoO_4$ nanotubes for oxygen evolution reaction, *New J. Chem.*, 2020, **44,** 17477–17482.

5 L. Chen, G.C. Xu, G. Xu, L. Zhang and H. Ding, Co-based coordination polymer-derived Co3S4 nanotube decorated with $NiMoO_4$ nanosheets for effective oxygen evolution reaction, *Int. J. Hydrogen Energy*, 2020, **45,** 30463–30472.

6 X.Q. Du, J.P. Fu and X.S. Zhang, $NiCo_2O_4$@$NiMoO_4$ Supported on Nickel Foam for Electrocatalytic Water Splitting, *ChemCatChem*, 2018, **10,** 5533–5540.

7 D. Cui, R.D. Zhao, J.Q. Dai, J. Xiang and F.F. Wu, A hybrid $NiCo_2O_4$@$NiMoO_4$ structure for overall water splitting and excellent hybrid energy storage, *Dalton Trans.*, 2020, **49,** 9668–9679.

8 M.B. Rammal and S. Omanovic, Synthesis and characterization of NiO, MoO_3, and

$NiMoO_4$ nanostructures through a green, facile method and their potential use as electrocatalysts for water splitting, *Mater. Chem. Phys.*, 2020, **225,** 123570.

9 Z.N. Wang, H. Wang, S. Ji, X.Y. Wang, P.X. Zhou, S.H. Huo, V. Linkov and R.F. Wang, A High Faraday Efficiency $NiMoO_4$ Nanosheet Array Catalyst by Adjusting the Hydrophilicity for Overall Water Splitting, *Chem. Eur. J.*, 2020, **26,** 12067–12074.

10 W. Gao, C. Wang, F.Y. Ma and D. Wen, Highly active electrocatalysts of CeO_2 modified $NiMoO_4$ nanosheet arrays towards water and urea oxidation reactions, *Electrochim. Acta*, 2019, **320,** 134608.

11 Y. Duan, Z.-Y. Yu, S.-J. Hu, X.-S. Zheng, C.-T. Zhang, H.-H. Ding, B.-C. Hu, Q.-Q. Fu, Z.-L. Yu, X. Zheng, J.-F. Zhu, M.-R. Gao and S.-H. Yu, Scaled-Up Synthesis of Amorphous NiFeMo Oxides and Their Rapid Surface Reconstruction for Superior Oxygen Evolution Catalysis, *Angew. Chem. Int. Ed.*, 2019, **58,** 15772–15777.

12 Y. Wang, Y.L. Zhu, S.L. Zhao, S.X. She, F.F. Zhang, Y. Chen, T. Williams, T. Gengenbach, L.H. Zu, H.Y. Mao, W. Zhou, Z.P. Shao, H.T. Wang, J. Tang, D.Y. Zhao and C. Selomulya, Anion Etching for Accessing Rapid and Deep Self-Reconstruction of Precatalysts for Water Oxidation, *Matter*, 2020, **3,** 2124–2137.

13 X. Liu, J.S. Meng, K. Ni, R.T. Guo, F.J. Xia, J.J. Xie, X. Li, B. Wen, P.J. Wu, M. Li, J.S. Wu, X.S. Wu, L.Q. Mai and D.Y. Zhao, Complete Reconstruction of Hydrate Pre-Catalysts for Ultrastable Water Electrolysis in Industrial-Concentration Alkali Media, *Cell Rep. Phys. Sci.*, 2020, **1,** 100241.

14 B.C. Moon, W.H. Choi, K.-H. Kim, D.G. Park, J.W. Choi and J.K. Kang, Ultrafine

Metallic Nickel Domains and Reduced Molybdenum States Improve Oxygen Evolution Reaction of NiFeMo Electrocatalysts, *Small,* 2019, **15,** 1804764.

15 M.A.Z.G. Sial, S. Baskaran, A. Jalil, S.H. Talib, H.F. Lin, Y.C. Yao, Q. Zhang, H.X. Qian, J.Z. Zou and X.R. Zeng, NiCoFe oxide amorphous nanohetrostructres for oxygen evolution reaction, *Int. J. Hydrogen Energy*, 2019, **44,** 22991–23001.

16 F. Qin, Z.H. Zhao, M. K. Alam, Y. Ni, F. Robles-Hernandez, L. Yu, S. Chen, Z.F. Ren, Z.M. Wang and J.M. Bao, Trimetallic NiFeMo for Overall Electrochemical Water Splitting with a Low Cell Voltage, *ACS Energy Lett.*, 2018, **3,** 546–554.

17 Z.H. Lv, Z.H. Li, X. Tan, Z.M. Li, R. Wang, M.J. Wen, X. Liu, G.X. Wang, G.W. Xie and L.H. Jiang, One-step electrodeposited NiFeMo hybrid film for efficient hydrogen production via urea electrolysis and water splitting, *Appl. Surf. Sci.*, 2021, **552,** 149514.

18 X.S. Su, Q.Q. Sun, J.J. Bai, Z.L. Wang and C. Zhao, Electrodeposition of porous MoO_4^{2-}-doped NiFe nanosheets for highly efficient electrocatalytic oxygen evolution reactions, *Electrochim. Acta*, 2018, **260,** 477–482.

19 K.-L. Yan, J.-F. Qin, Z.-Z. Liu, B. Dong, J.-Q. Chi, W.-K. Gao, J.-H. Lin, Y.-M. Chai and C.-G. Liu, Organic-inorganic hybrids-directed ternary NiFeMoS anemone-like nanorods with scaly surface supported on nickel foam for efficient overall water splitting, *Chem. Eng. J.*, 2018, **334,** 922–931.